Operating characteristics study of a dual-opposed free-piston Stirling generator

Haojie Sun[a,b], Guoyao Yu[a,c,1], Dan Zhao[d], Shunmin Zhu [a,e,1], Wei Dai[a,b], Ercang Luo[a,b]

a. Key Laboratory of Cryogenics, Technical Institute of Physics and Chemistry, Chinese Academy of Sciences, Beijing 100190, China

b. University of Chinese Academy of Sciences, Beijing 100049, China

c. Institute of Optical Physics and Engineering Technology, Qilu Zhongke, Jinan 251000, China

d. Department of Mechanical Engineering, Faculty of Engineering, University of Canterbury, Private Bag 4800, Christchurch 8140, New Zealand

e. Department of Engineering, Durham University, Durham DH1 3LE, UK

Abstract:

Dual-opposed Free-piston Stirling generators (dual-opposed FPSGs) offer advantages of reduced vibration and increased power density, making them promising candidates for space and distributed energy applications. So far, operational characteristics of the dual-opposed FPSG have yet to be completely understood. This study focuses on a 3 kW dual-opposed FPSG prototype designed to integrate heat pipes. Through computational fluid dynamics and thermoacoustic analysis, a novel hot end heat exchanger with evenly-distributed heat pipe bore was discovered to deliver 12 kW heating power with a gas-solid temperature difference of 21 K. Subsequently effort combined thermoacoustically-based calculations with experiments to investigate the impact of two electrical connection methods of linear alternators on FPSG performance. Experimental results validated the numerical model, showing heat-to-electricity efficiency deviations within 5% under different electrical connection modes. The FPSG consistently achieved its rated power in both series and parallel connection modes, exhibiting a thermal-to-electric efficiency of 25.2%. Notably, the series connection mode demonstrates superior sensitivity and consistency compared to parallel connection. Further experiments revealed that charge pressure, load resistance and external capacitance all exerts limited impact on the consistency, while external capacitance significantly influenced acoustic impedance. This resulted in an enhancement in both hot-end wall temperature and heat-to-electricity efficiency, while minimizing power piston displacement and damping temperature when

[1] Corresponding author.
E-mails address: gyyu@mail.ipc.ac.cn (G.Yu), zhushunmin@mail.ipc.ac.cn (S. Zhu)

resonating with the inductance.

Keywords: dual-opposed; free-piston Stirling generator; electrical connection mode; operating characteristics

Nomenclature

symbols	
A	cross-sectional area, m^2
e	internal energy, W
Bl	transduction coefficient, V•s/m
C	compliance, m^3/Pa
F	pressure drop due to viscosity, Pa
I	current, A
i	imaginary unit
K	stiffness, N/m
L	inertance, kg/m^4
l	length, m
m	moving mass, kg
n	amount of substance, mol
p	Oscillating pressure, Pa
P	pressure, Pa
q	axial heat flux, W
Q	heat exchange rate, W
R	gas constant, J/(mol·K)
R_m	damping coefficient, N·s/m
R_e	resistance, Ω
T	Temperature, K
u	velocity, m/s
U	volume flow rate, m^3/s
W_e	electrical power, W
Z	Acoustic impedance, Pa·m^3/s

Greek symbols

η	efficiency, %
θ	phase angle, °
ω	angular frequency, 1/s

Subscripts

b	bounce chamber
c	compression chamber
disp	displacer
e	expansion chamber
h	Hot end heat exchanger
H-E	heat-to-electricity
i	internal
mp	Mechanism of piston
serial	series connection
out	outlet
parallel	parallel connection
p/pist	piston
w	transfer with solid

1. Introduction

In light of intense concerns about energy crises and the greenhouse effect worldwide, the exploration of renewable and sustainable energy conversion technology is an imperative but challenging task. Power generation is one of the most common energy conversion technologies, which gains flexible and reliable electrical power from primary energy. A free-piston Stirling generator (FPSG), which ingeniously couples a free-piston Stirling engine (FPSE) with a linear alternator, is an acoustic resonated system capable of converting heat to electricity efficiently. Due to its promising advantage of compact structure, extremely long lifetime, high thermal efficiency, high reliability, and good adaptivity to various heat sources, the FPSG can be used in a large range of applications, such as space nuclear power generation [1, 2], micro-combined heat and power systems [3, 4], and concentrated solar power generation [5, 6].

While single-piston FPSGs have been extensively studied, their operational characteristics are well understood [7-9]. However, the introduction of the dual-opposed configuration has introduced new complexities that remain poorly comprehended. Unlike single-piston FPSGs, dual-opposed FPSGs feature two independent linear alternators placed opposite each other, posing challenges in external electrical connection design. Within the NASA-funded Space Power (SP)-100 program, a Space Power Demonstrator Engine (SPDE) was first developed to evaluate the viability of Stirling technologies to a space nuclear power generation system [10]. The SPDE consists of two 12.5 kW single-piston FPSG submodules in an opposed inline configuration, and the two submodules share an expansion chamber. The system is heated by a molten salt circulation loop, which is used to simulate a heat source with a temperature of 650 K. The cold end is cooled by a water/glycol circulation loop with a cooling temperature of 325 K. The operating frequency of the SPDE is 100 Hz and the displacement of the power piston is 20 mm, resulting in a 22 % heat-to-electricity efficiency. Orbital Sciences Corporation (OSC) [11] and Lockheed Martin (LM) [12] adopted the dual-opposed configuration to reduce the vibration of a system that integrates two 55-W TDC (Technology Demonstration Convertor) units developed by Stirling Technology Company. The specific power of the system integrated by OSC reached 8 W/kg and the heat-to-electricity efficiency exceeded 20%. The specific power of the LM's system is 4.2 W/kg and the output power is 112 W. In 2002, LM Corporation developed a 100-W FPSG for deep space exploration and Mars exploration. The system also

uses a dual-opposed configuration and uses metal beryllium as the shell and heat dissipation structure. In experiments, the initial output is 116 W, the heat-to-electricity efficiency is 22% and the specific power is 3.5 W/kg [13]. In a project performed at the NASA Glenn Research Center [14], the researchers used electric cartridge heaters for thermal input to test two EG-1000 FPSGs, which are placed opposite. Under the temperature ratio of 823 K/313 K, 2240 W of electric power could be generated, and the efficiency is 28.6%. Subsequently, the heater head structure was refurbished to improve the heat exchange efficiency, and the original electric heating system was replaced with a sodium-potassium (NaK) heating circuit. Under the same temperature ratio, the generator output power reached 2372 W, and the efficiency increased to 32% [15, 16]. As of 2010, Sunpower developed a 12-kW dual-opposed FPSG based on the EG-1000. The two FPSGs share a common heater and a common expansion space, with the hot head temperature set at 850 K and the room temperature end at 375 K. The output power and heat-to-electricity efficiency of the two generators are 6109 W@26.5% and 6048 W@24.4%, respectively [17, 18]. It is found that the consistency of the two FPSGs still needs to be ameliorated. In 2015, NASA developed a dual opposed FPSG based on heat pipes. The whole system has a mass of 406 kg, a maximum diameter of 1.1 m, and a total length of 3 m. The FPSG can output 183 W of electric power at 50% relative Carnot efficiency [19]. Since then, several tests have been carried out. The output power of a single FPSG is 90 W, the heat-to-electricity efficiency is 35%, and the overall efficiency of the system is 25% [20]. Lin et al. [21] also developed an FPSG based on a heat pipe composed of two dual-opposed FPSGs. The system test results show that the power output exceeds 300 W, and the overall efficiency is 7.36%.

The above progresses preliminarily demonstrate that the dual-opposed configuration in free-piston Stirling systems is conducive to not only reducing vibration but also increasing the overall power density. Within such a configuration, two independent linear alternators are placed opposite each other, rendering a crucial issue of external electrical connection. Taking a moving-coil linear compressor for instance, two identical compressor halves mounted back-to-back but sharing a common compression space have been proven to be capable of reducing vibration [22, 23]. Park et al. [24] developed a 1 kW-class free-piston Stirling cryocooler (FPSC) driven by a dual-opposed linear compressor, with the two linear compressor halves connected

in parallel electrical connection to make the pistons move in anti-phase synchronization. Each linear compressor half has a rated voltage, current, and resultant thrust of 380 Vrms, 15.8 Arms, and 135 N A^{-1}, respectively, with a frequency set at 45 Hz, closing to its natural frequency. Unlike an actively manipulated FPSC, the electrical parameters such as operating frequency, current, and voltage are intrinsically determined by the FPSG itself. Therefore, the external electrical design of an FPSG that incorporates two dual-opposed linear alternator halves is more complicated than that of an FPSC that integrates two linear compressor halves. In another work performed by Park et al. [25], they designed a kW-class FPSE for micro-combined heat and power application, which utilized an FPSE to drive a dual-opposed type linear alternator. In their experimental setup, two independent linear alternator halves are connected in series, but the detailed external electrical design of the entire system is not revealed, let alone its characteristics.

Efforts to address these challenges have been undertaken by various researchers, resulting in the development of several dual-opposed FPSG prototypes. However, the specific characteristics and optimal electrical connection methods of these systems remain ambiguous. In a typical dual-opposed FPSG, two engine heads generally share a common expansion chamber, and the acoustic power that flows bilaterally into the expansion chamber interacts with each other. This mutual effect inevitably makes the electrical design of the dual-opposed FPSG more complex than that of an FPSG with a single engine head. Unfortunately, the electrical connection of the two identical linear alternators in dual-opposed FPSGs has not been specifically studied, and the characteristics are still ambiguous. Therefore, comparing the two alternative electrical connection methods (series electrical connection and parallel electrical connection) for the linear alternators and choosing an optimum one is one of the purposes of this work. Moreover, though the rudimentary operating characteristics of single-piston FPSGs have been fully understood to date, the operating characteristics of dual-opposed FPSGs remain poorly comprehended due to the more complex acoustic interaction within it. A comprehensive experimental study aiming to reveal the influence of key operating parameters on the operation and performance of the dual-opposed FPSG is lacking. To contribute to filling this research gap is another purpose of this work.

This study aims to address this gap by developing a 3 kW-class dual-opposed FPSG prototype and comparing the performance of two electrical connection methods for the linear alternators: series and parallel connection. Additionally, the study investigates the effects of key operating parameters—including charge pressure, load resistance, and external capacitance—on the system's operation and performance. Experimental investigations focus on crucial parameters such as hot-end heat exchanger wall temperature, heat-to-electricity efficiency, piston displacement, onset temperature, and damping temperature. The findings of this study are expected to contribute to a better understanding of dual-opposed FPSG operation and performance, guiding future advancements in this field.

2. System configuration and measurements

2.1 Apparatus description

Fig. 1 presents a schematic diagram of the 3 kW-class dual-opposed FPSG prototype. As depicted in Fig. 1, the 3 kW FPSG consists of two identical 1.5 kW single-piston FPSGs with a shared expansion chamber. Each single-piston FPSG comprises a displacer (supported by four identical pieces of planar springs), a power piston, outer stators (with coil encapsulated in the outer stator), permanent magnets, a compression chamber, an ambient heat exchanger, a regenerator, a hot end heat exchanger, and a shared expansion chamber. The whole system is filled with pressurized helium. It should be noted that this prototype is designed to be capable of integrating heat pipes to facilitate the heat transfer between remote heat source and the hot end heat exchanger. Fig. 2 is a photograph of the dual-opposed FPSG prototype, and Table 1 lists the detailed dimensions of each component of the dual-opposed FPSG.
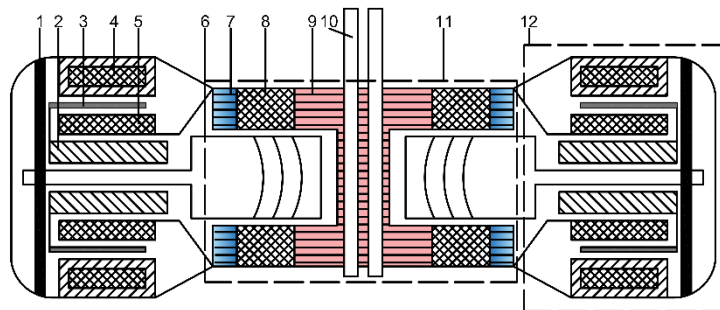
1- planar spring, 2-power piston, 3-permanent magnet, 4-outer stator, 5-inner stator, 6-compression chamber, 7-ambient heat exchanger, 8-regenerator, 9-hot end heat exchanger, 10-heat pipes / electric cartridge heaters, 11-FPSE, 12-linear alternator

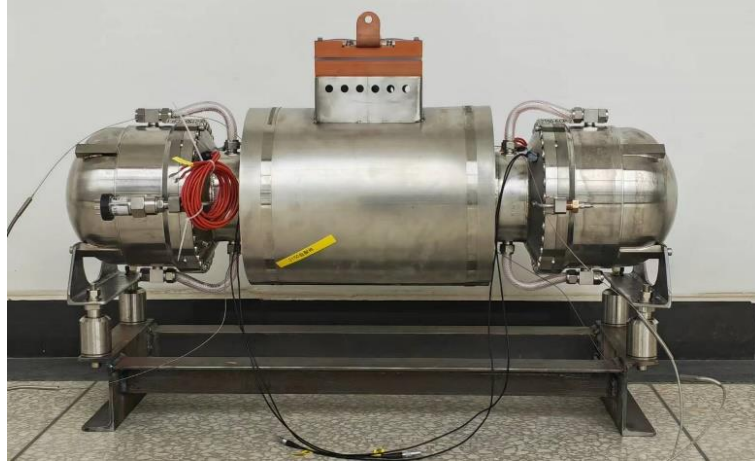Figure 1 Schematic diagram of the dual-opposed FPSG prototype.

Figure 2 Photograph of the 3 kW dual-opposed FPSG prototype.

Table 1 Main parameters of the 3 kW dual-opposed FPSG.

Component name	details	value
Hot end heat exchanger	Length /m	0.024
	Flow area /m^2	1.116×10^{-3}
Regenerator	Length /m	0.045
	Equivalent area /m^2	5.236×10^{-3}
	Porosity /%	88.5
	Wire diameter /m	1.7×10^{-5}
Ambient heat exchanger	Length /m	0.035
	Flow area /m^2	3.619×10^{-4}
Displacer	Moving mass /kg	0.904
	Stressed area facing the compression space /m^2	5.027×10^{-3}
	Stressed area facing the expansion space / m^2	5.518×10^{-3}
	Spring constant / (N/m)	2.7×10^5
Displacer rod	Area /m^2	4.909×10^{-4}
Compression chamber	Volume /m^3	9.3×10^{-5}
Expansion chamber	Volume /m^3	1.9×10^{-4}
Alternator	Transduction coefficient / (N/A)	120
	Internal electric resistance /Ω	1.17
	Internal inductance / H	5.85×10^{-2}
	Spring constant / (N/m)	7.1×10^4
Power piston	Stressed area (excluding the displacer rod area) /m^2	5.027×10^{-3}
	Moving mass /kg	2.08

To evaluate the performance and operating characteristics of the dual-opposed FPSG prototype, a test rig for the prototype was built. The test rig includes a 3 kW-class FPSG

prototype, a heating sub-system, a cooling sub-system, an electric load sub-system, and a measurement sub-system, as shown in Fig. 3. The heating sub-system is composed of a power meter (model AN8711P from Ainuo, with an error of ± 0.4% indication error plus ± 0.4% full scale), a voltage regulator, and 12 electric cartridge heaters that distributed in two hot end heat exchangers uniformly. Herein, electric cartridge heaters each with a diameter of 16 mm are chosen preliminarily instead of the heat pipes to supply heat to the hot end heat exchanger. By virtue of the electrical heating, the heat input sub-system guarantees an accurate and even heating power to the dual-opposed FPSG. For the cooling sub-system, the water circulates between a water chilling unit and the ambient heat exchanger. In experiments, the inlet cooling water temperature of the ambient heat exchanger is set at 20 °C. The load sub-system is an external electric circuit including a rheostat and a capacitor. The rheostat and capacitor play roles in consuming the power generated by the two linear alternators meanwhile achieving the electrical resonance of the electric circuit.
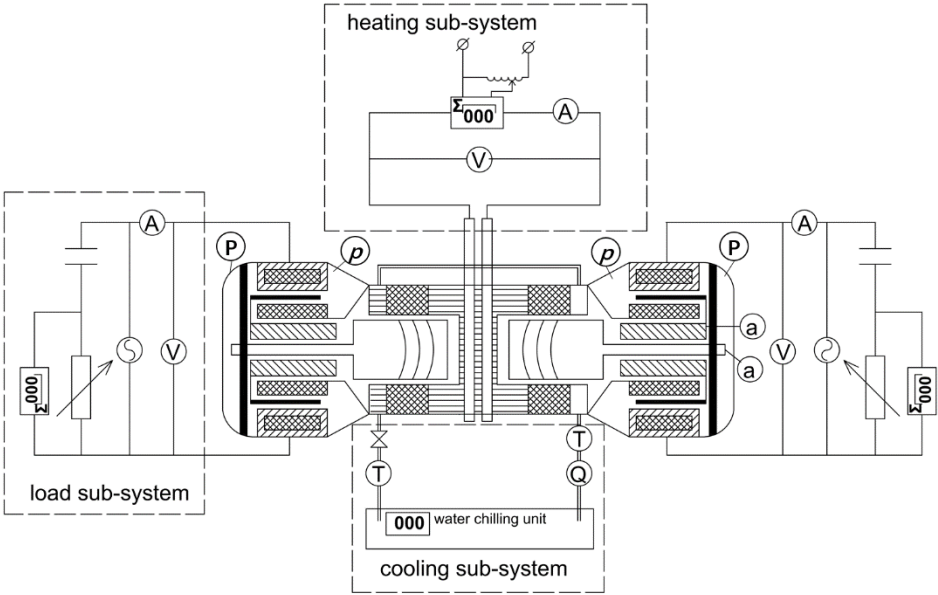

Figure 3 Schematic diagram of the dual-opposed FPSG test rig system.

2.2 Hot end heat exchanger design

As mentioned before, the hot end heat exchanger of the dual-opposed FPSG prototype in this work is designed to be capable of integrating heat pipes. Therefore, to ensure sufficient gas-solid heat exchange area and a larger installation diameter of high-temperature heat pipes, the design of hot end heat exchanger is quite different from conventional ones that use electric

heating or direct flue gas heating. The unique layout of the hot end heat exchanger is illustrated in Fig. 4, and it encompasses twelve through-thickness holes to accommodate the high-temperature heat pipes and two radial bores to form the common expansion space. The core of the hot end heat exchanger is made of copper with thin fins to improve the internal temperature uniformity of working gas.
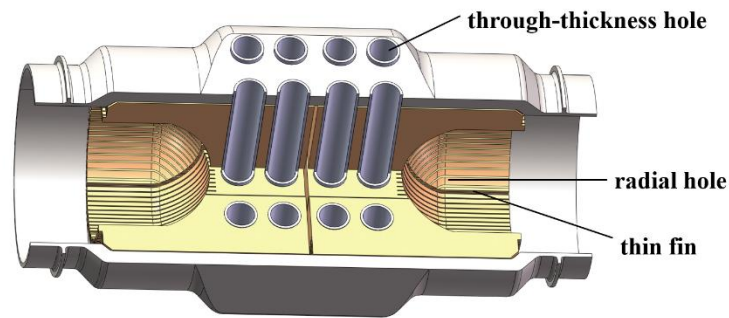

Figure 4 Cut-away view of the hot end heat exchanger of the 3kW dual-opposed FPSG prototype.

Investigating the temperature distribution within the hot end heat exchanger necessitates a thorough understanding of fluid-solid interactions. Therefore, a liquid-solid coupling model was developed using ANSYS Fluent 19.0. Gedeon et al. verified Iguchi's proposal that the fluid flow remains unaffected by prior cycles, exhibiting characteristics akin to steady-state flow [26, 27]. Consequently, this study employs steady-state flow simulations to determine the heat transfer and resistance coefficients pertinent to the hot end heat exchanger. The grid diagram is presented in Fig 5(a). A representative quarter-section of the heat exchanger was modeled, employing Fluent Meshing for grid partitioning. Through meticulous grid independence analysis, a three-layer boundary layer was established, resulting in a total grid count of 2,954,000 with a grid orthogonality quality of 0.1. The schematic diagram of boundary conditions is depicted in Fig 5(b). The simulation considers a helium gas working medium at 5 MPa, with a mass flow inlet of 0.055 kg/s and an inlet temperature of 821 K. The outlet is set as a pressure outlet with a static pressure of 5 MPa. The heat pipe wall maintains a constant heat flow boundary with a total heat flow of 3 kW, while the hot end heat exchanger shell is thermally insulated. User Defined Functions (UDF) were utilized to specify the physical properties of helium, copper, and stainless steel. Turbulence modeling adopts the k-omega

standard, with computational solutions facilitated by the SIMPLE algorithm. Additionally, the second-order upwind format enhances computational precision.
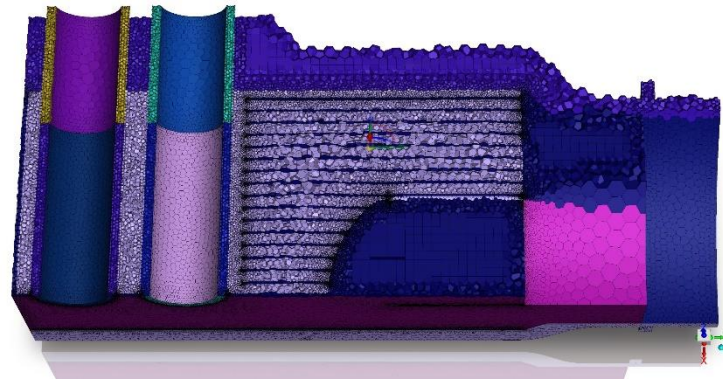
(a)
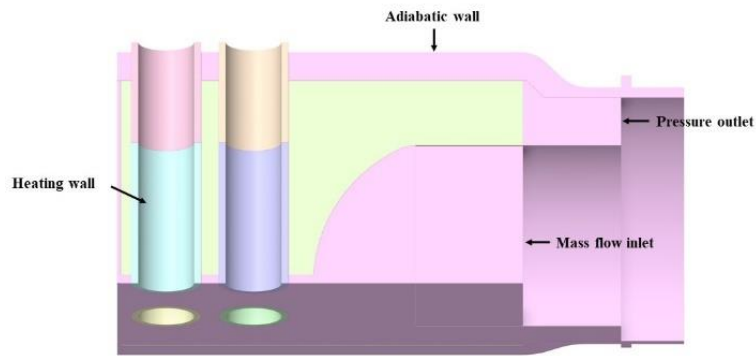
(b)

Figure 5 Grid diagram (a) and schematic diagram of boundary conditions of the hot end heat exchanger.

The temperature gradient within the solid material and the corresponding temperature distribution of the solid and adjacent working gas in the hot end heat exchanger are depicted in Fig. 6(a) and Fig. 6(b), respectively. Note that the surface temperature of the hot end heat exchanger is 907 K, while the mean temperature of copper is 842 K with a gas-solid temperature difference of 21 K. Due to the high thermal conductivity of copper, the hot end heater end shows good thermal diffusion and temperature uniformity. Furthermore, the working gas pressure drop between the inlet and the outlet of the hot end exchanger is 27 kPa, comparable to that of a single FPSG.
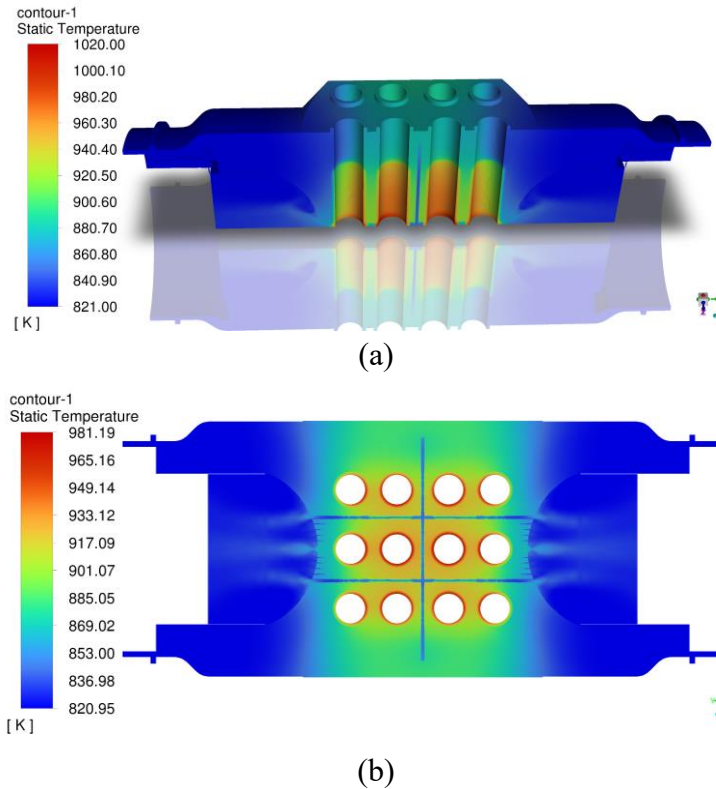
(a)

(b)

Figure 6 Temperature distribution of the solid and adjacent working gas of the hot end heat exchanger: (a) solid (b) solid and working gas.

2.3 Measurements

As for the measurement sub-system, voltage transducers, current probes, and power meters are deployed at the load circuit of the two linear alternators to monitor the output electric parameters of each FPSG. It should be noted that the position of the current probes and voltage transducers in serial connection condition of the two alternators are different from that in parallel connection condition of the two alternators, which will be introduced in detail in Section 3. The surface temperature of the hot end heat exchanger is measured by four K-type thermocouples (with accuracy class 1) that fastened to the center of adjacent four heater cartridges. The mean pressure of the system is measured by using two pressure transducers that are installed in the bounce space of each FPSG. Meanwhile, two high-precision dynamic pressure sensors (PCB 113B26) are mounted in each compression space to measure the dynamic pressure and pressure ratio therein, respectively. The cooling water circulation loop is equipped with two PT100 thermometers and a turbine flowmeter to measure the inlet and outlet temperature (at the AHX) and volume flow of the cooling water, respectively. These three parameters are used to calculate the heat loss of the whole system. In addition, the displacement amplitude and phase of each displacer and each power piston are captured by accelerometers

(PCB M353B18), respectively. The signals of pressure transducers, dynamic pressure sensors, and accelerometers are collected simultaneously by an 8-channel data acquisition system (National Instruments PXI 4472B). The other signals are logged by an Agilent Data Acquisition Unit (34972A).

Direct measurement parameters such as oscillating pressure, current, voltage, electrical power, and temperature are assessed for experimental errors based on the maximum permissible error of the sensors. In contrast, indirect measurement parameters like thermal-to-electric efficiency undergo error calculation using the error transfer formula, as outlined in reference [28]. The experimental errors of experimental parameters are listed in Table 2.

Table 2 Experimental errors of experimental parameters

Parameter	Sensor type	Experimental error
Surface temperature of the hot end heat exchanger	K-type thermocouple	± 1.5 K
Oscillating pressure	Dynamic pressure sensor PCB 113b26	34 kPa
Temperature of cooling water	PT100 thermometer	0.15 K
Mean pressure	Pressure transducer	25 kPa
Volume flow of the cooling water	Turbine flowmeter	0.02 m3/s
Acceleration of moving parts	Accelerometer PCB M353B18	49 m/s
Current of generators	Current probe PINTECH PT-2710	0.2 A
Voltage of generators	Voltage transducer PINTECH N1008b,	6 V
Power of generator	Power meter NAPUI PM9840	$\pm 0.4\%$ indication error
Heating power	Power meter NAPUI PM9840	$\pm 0.4\%$ indication error
Heat-to-electric efficiency	-	0.4%

3. Two electrical connection modes of linear alternators

Generally speaking, acoustic and electrical resonance are inherent properties of FPSG. The external circuit connection method of the two alternators determines the operation characteristics of the dual-opposed FPSG. Fig. 7 presents the circuit diagrams of the two electrical connection modes. In Fig. 7(a), the two alternators are connected in series. Each linear

alternator is connected in parallel with a voltmeter firstly, then they connect a current probe, an external resistance, and a capacitance in series. Due to the difference between static and kinetic friction of pistons and displacers, an excitation power supply with an output voltage of 220 V and a frequency of 50 Hz is used to trigger the FPSG during the onset process. In Fig. 7(b), the two alternators are connected in parallel. In each parallel branch of the circuit that includes a linear alternator, the linear alternator connects with a current probe in series, and then the two parallel branches are connected in parallel with a voltmeter, and an excitation power supply. Finally, the above circuit connects with an external resistance and a capacitance in series.
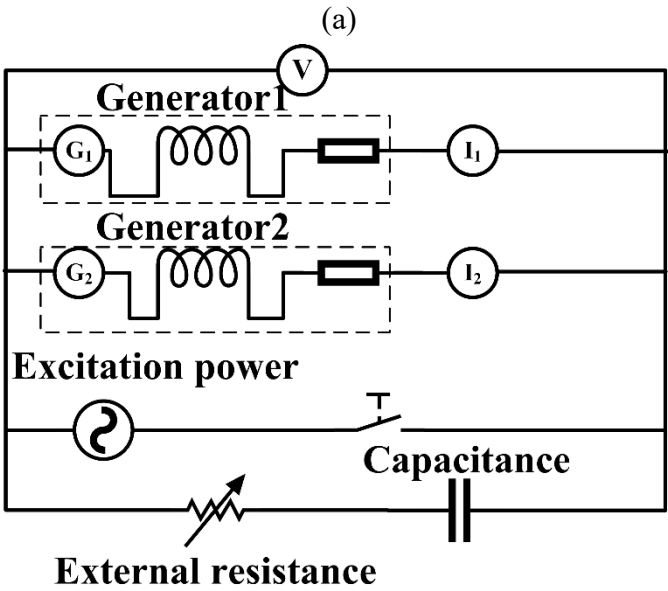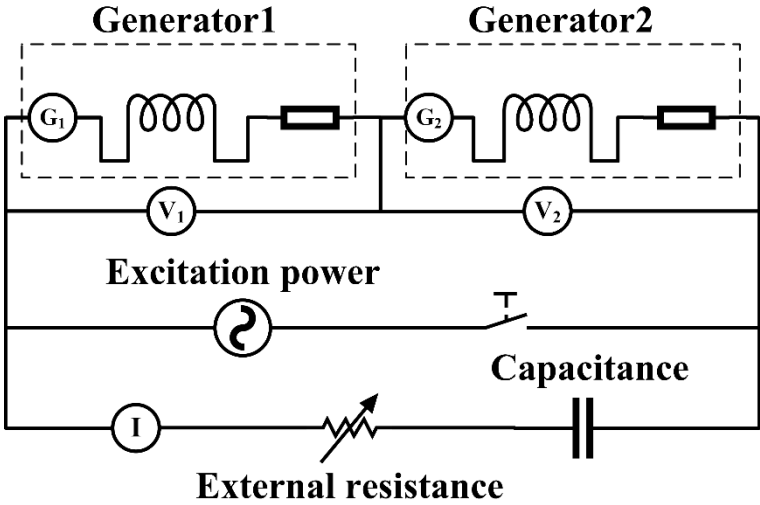
Figure 7 Circuit diagrams of the two electrical connection modes of the two linear alternators:(a) series connection, and (b) parallel connection.

From the perspective of thermoacoustics, the output acoustic impedance of the FPSE is identical with the acoustic impedance of the linear alternator. The acoustic impedance of the linear alternator can be deduced by the force balance equation of the power piston, shown as:

$$\hat{P}_c A_p - \hat{P}_b A_p = \hat{I}Bl + \frac{K_p \hat{u}}{i\omega} + R_{mp}\hat{u} + m_p i\omega\hat{u} \tag{1}$$

where $\hat{P}_c$ and $\hat{P}_b$ represent the oscillating pressure amplitude in the compression chamber and bounce space, respectively; A_P is the equivalent cross-sectional area of the power piston, excluding the displacer rod area; Bl, $\hat{u}$, R_{mp}, K_p and m_p denote the transduction coefficient, velocity, mechanical damping, total stiffness, and mass of the piston, respectively; $\hat{I}$ is the current pass through the coil.

Meanwhile, the electric balance equation for the two alternators that connect in series is expressed as follows:

$$2Bl\hat{u} = \hat{I}\left(R_{e-serial} + 2R_i + i(2\omega L - \frac{1}{\omega C_{serial}}) \right) \tag{2}$$

where $R_{e-serial}$, R_i, L, and C_{serial} represent the external resistance, internal resistance, internal inductance, and external capacitance.

Combining Eq. (1) and Eq. (2), we obtain:

$$(\hat{P}_c - \hat{P}_b)A_p = \frac{Bl^2\hat{u}}{\frac{1}{2}\mathrm{R}_{e-serial} + R_i + i(\omega L - \frac{1}{2\omega C_{serial}})} + \frac{K_p\hat{u}}{i\omega} + R_{mp}\hat{u} + m_p i\omega\hat{u} \tag{3}$$

If the both sides of Eq. (3) are divided by velocity $\hat{u}$, Eq. (3) is rewritten in the form of:

$$\left[Z_c A_p A_p - Z_b A_p A_p \right]_{serial} = \left[\frac{Bl^2(\frac{1}{2}\mathrm{R}_{e-serial} + R_i)}{(\frac{1}{2}\mathrm{R}_{e-serial} + R_i)^2 + (\omega L - \frac{1}{2\omega C_{serial}})^2} + R_{mp} \right]$$
$$+ \left[m_p\omega - \frac{K_p}{\omega} - \frac{Bl^2(\omega L - \frac{1}{2\omega C_{serial}})}{(\frac{1}{2}\mathrm{R}_{e-serial} + R_i)^2 + (\omega L - \frac{1}{2\omega C_{serial}})^2} \right]i \tag{4}$$

where Z denotes local acoustic impedance, which is the ratio of the oscillating pressure and flow volume rate. The physical meaning of this equation is very apparent, i.e., the output acoustic impedance of the FPSE equates to the acoustic impedance of the linear alternator.

Likewise, the electric balance equation for the two alternators that connect in parallel is:

$$Bl\hat{u} = \hat{I}\left(2R_{e-parallel} + R_i + i(\omega L - \frac{2}{\omega C_{parallel}})\right) \tag{5}$$

Combining Eq. (5) with Eq. (1), we obtain the acoustic impedance equation for the two alternators that connect in parallel:

$$
\left[Z_c A_p A_p - Z_b A_p A_p\right]_{parallel} = \left[\frac{Bl^2(2R_{e-parallel} + R_i)}{(2R_{e-parallel} + R_i)^2 + (\omega L - \frac{2}{\omega C_{parallel}})^2} + R_{mp}\right]
$$
$$
+ \left[m_p\omega - \frac{K_p}{\omega} - \frac{Bl^2(\omega L - \frac{2}{\omega C_{parallel}})}{(2R_{e-parallel} + R_i)^2 + (\omega L - \frac{2}{\omega C_{parallel}})^2}\right]i \tag{6}
$$

Assuming that the structural parameters and operating conditions of the FPSG remain unchanged with the shift of the electrical connection modes of the two alternators, namely the output acoustic impedance of the FPSE keeps constant, we have:

$$\text{Re}\left[Z_c A_p A_p - Z_b A_p A_p\right]_{parallel} = \text{Re}\left[Z_c A_p A_p - Z_b A_p A_p\right]_{serial} \tag{7}$$

$$\text{Im}\left[Z_c A_p A_p - Z_b A_p A_p\right]_{parallel} = \text{Im}\left[Z_c A_p A_p - Z_b A_p A_p\right]_{serial} \tag{8}$$

Namely:

$$
\left[\frac{Bl^2(2R_{e-parallel} + R_i)}{(2R_{e-parallel} + R_i)^2 + (\omega L - \frac{2}{\omega C_{parallel}})^2} + R_{mp}\right] = \left[\frac{Bl^2(\frac{1}{2}R_{e-serial} + R_i)}{(\frac{1}{2}R_{e-serial} + R_i)^2 + (\omega L - \frac{1}{2\omega C_{serial}})^2} + R_{mp}\right]
$$
$$(9)$$

$$
\left[m_p\omega - \frac{K_p}{\omega} - \frac{Bl^2(\omega L - \frac{2}{\omega C_{parallel}})}{(2R_{e-parallel} + R_i)^2 + (\omega L - \frac{2}{\omega C_{parallel}})^2}\right] = \left[m_p\omega - \frac{K_p}{\omega} - \frac{Bl^2(\omega L - \frac{1}{2\omega C_{serial}})}{(\frac{1}{2}R_{e-serial} + R_i)^2 + (\omega L - \frac{1}{2\omega C_{serial}})^2}\right]
$$

Solving Eq. (7) and Eq. (8), the relation between external resistance of parallel connection of the two alternators and that of series connection of the two alternators is obtained accordingly, as shown in Eq. (11):

$$\mathrm{R}_{e-serial} = 4\,\mathrm{R}_{e-parallel} \tag{11}$$

The relation for external capacitance is also given in Eq. (12):

$$C_{serial} = \frac{1}{4} C_{parallel} \tag{12}$$

When the external circuit of the FPSG satisfies these two equations, both series connection mode and parallel connection mode suffice to provide the desired electric impedance. However, it is rather difficult to achieve this ideal state in practice due to the in-consistency of structural parameters between the two FPSGs and the difficulty in instant adjustment of capacitance.

In experiments, the capacitances in series connection mode and parallel connection mode are set to be 32.6 μF and 135.4 μF, respectively. The flowchart outlining the calculation methodology for dual-opposed FPSGs is presented in Fig. 8. The acoustic impedance of the FPSE is calculated by using commercial software SAGE [29], which is a three-order thermodynamic analysis tool for Stirling engine modelling, design, and optimization. The governing equations of the FPSE are typically represented in a standard format, denoted by Eq. (13) to Eq. (15). The detailed formulations for flow and heat transfer are outlined in reference [30].

$$\frac{\partial \rho A}{\partial t} + \frac{\partial \rho u A}{\partial x} = 0 \tag{13}$$

$$\frac{\partial \rho u A}{\partial t} + \frac{\partial u \rho u A}{\partial x} + \frac{\partial P}{\partial x} A - FA = 0 \tag{14}$$

$$\frac{\partial \rho e A}{\partial t} + P \frac{\partial A}{\partial t} + \frac{\partial}{\partial x}(u \rho e A + u P A + q) - Q_w = 0 \tag{15}$$

In these equations, the symbols A, u, x, P, q, F, e, and Q_w correspond to cross-sectional area, velocity, axial position, pressure, axial heat flux, pressure drop due to viscosity, internal energy, and heat transfer between the fluid flow and solid surfaces, respectively.
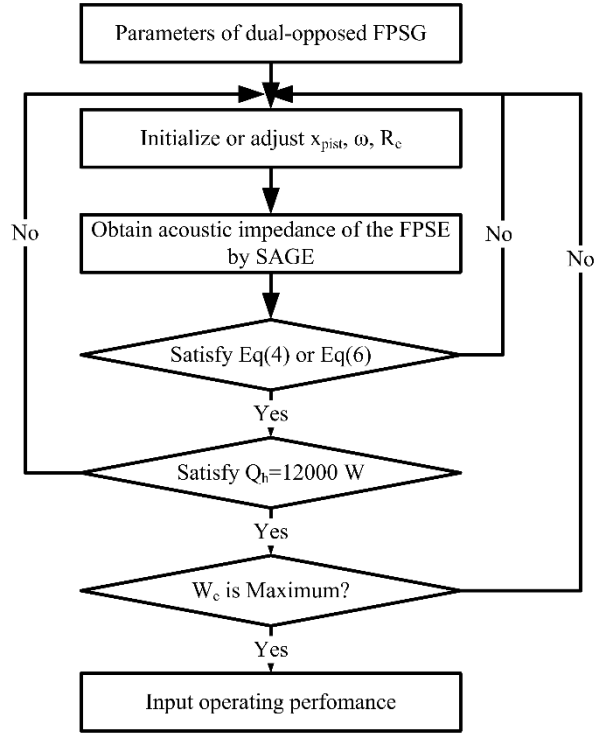
```
┌─────────────────────────────────────┐
│   Parameters of dual-opposed FPSG    │
└─────────────────────────────────────┘
                   ↓
┌─────────────────────────────────────┐
│   Initialize or adjust xpist, ω, Rc  │
└─────────────────────────────────────┘
                   ↓
┌─────────────────────────────────────┐
│  Obtain acoustic impedance of the    │
│        FPSE by SAGE                   │
└─────────────────────────────────────┘
                   ↓
        ◇ Satisfy Eq(4) or Eq(6) ◇   No
                  Yes
        ◇ Satisfy Qh=12000 W ◇
                  Yes
        ◇ Wc is Maximum? ◇
                  Yes
┌─────────────────────────────────────┐
│       Input operating perfomance     │
└─────────────────────────────────────┘
```

Figure 8 Flowchart outlining the calculation methodology for dual-opposed FPSGs.

The acoustic impedance of the linear alternator is obtained by using Eq. (4) or Eq. (6) according to the electrical connection method. When the operating parameters are regulated to make both Eq. (4) and Eq. (6) satisfied, the FPSE and linear alternator are deemed well-matched. Finally, the state parameters of the whole FPSG are calculated, including the displacements of the power piston and displacer, the dynamic pressure, the first-order volume flow rate, and the corresponding heat-to-electricity efficiency.

4. Results and discussion

4.1 Comparison of the two electrical connection methods

We performed simulations and experiments on the dual-opposed FPSG, considering two different linear alternators electrical connection modes, i.e., parallel connection and series connection, under a given heating power of 12 kW. Table 3 lists the detailed operating parameters of the dual-opposed FPSG in experiments and simulations. As seen in Table 3, the FPSG reaches its rated power in both series connection and parallel connection modes with an efficiency of 25.2% in experiments. When the two linear alternators are connected in series, the system starts up oscillation at a hot end heat exchanger wall temperature of 291 °C (the corresponding gas temperature in the expansion chamber is 205 ℃, inferred from 2.2) under

an external resistance of 135 Ω. Besides, a maximum output power of 3018 W is achieved on the dual-opposed FPSG under an external resistance of 60 Ω. Regarding the comparison between experiments and simulations, a deviation of 3.19% on the heat-to-electricity is obtained. In addition, it's encouraging to see that the displacement amplitude difference between two power pistons is 0.11 mm, and the phase difference is 0.5°. As for the displacer, the amplitude difference is 0.03 mm, and the phase difference is 3°. A fast evaluation of this inconsistency has been done from the perspective of momentum conservation. The results reveal that the vibration amplitude of single-piston FPSG shell is 0.3 mm while that of the dual-opposed FPSG is only 0.006 mm, indicating a good vibration suppression by adopting dual-opposed configuration.

Table 4 presents a comprehensive comparison between the outcomes of our experiment and those reported in existing studies. Our results demonstrate that the heat-to-electricity efficiency of the dual-opposed FPSG at the kilowatt electricity capacity level is relatively higher compared to most prior studies. Furthermore, our dual-opposed FPSG exhibits long-term stable operation, with a current operating time exceeding 200 hours.

Table 3 Detailed operating parameters of the dual-opposed FPSG in experiments and calculations.

electrical connection methods	Method	Heating power (kW)	Frequency (Hz)	X_{pist} (mm)	X_{disp} (mm)	$\theta_{p\text{-}p}$ (°)	$\theta_{d\text{-}d}$ (°)	Voltage (V)	Current (A)	W_e (W)	R_e (Ω)	$\eta_{H\text{-}E}$ (%)
Series	Simulation	12	79.44	6.98/6.98	6.07/6.07	0	0	302.9	7.16	3118	60.9	25.98
Series	Experiment	12	79.22	7.1/7.21	7.38/7.35	0.5	3	304/309	7.09	3018	60	25.15
Parallel	Simulation	12	79.66	6.98/6.98	6.10/6.10	0	0	302.9	14.17	3105	15.47	25.88
Parallel	Experiment	12	79.43	7.07/7.22	7.36/7.37	0.9	3.8	300.7	14.17	3022	15	25.18

Table 4 Comparison between the outcomes of this experiment and those reported in existing studies.

author/ company	Method	Hot end temperature(K)	W_e (W)	cold-end temperature(K)	$\eta_{H\text{-}E}$ (%)	reference
Xiao et al.	simulation	873	3920	297	46.6	[31]
Chen et al.	experiment	673	3200	297	22.10	[32]
Lin et al.	experiment	873	300	300	7.36	[21]
MTI	experiment	630	17000	325	22	[33]
Qi et al.	simulation	1200	8900	300	21.69	[34]
Sunpower	experiment	824	12000	375	26.50	[19]
Sunpower	experiment	840	183	-	35	[20]
NASA	experiment	823	240	313	28.60	[14]
LM	experiment	923	116	333	22	[13]
Our research	experiment	898	3022	300	25.18	

When the two linear alternators are connected in parallel, the system onsets at a hot end heat exchanger wall temperature of 246 °C (the corresponding gas temperature in the expansion chamber is 160 ℃, inferred from 2.2) under an external resistance of 67 Ω. The reason why the onset temperature under the parallel connection mode is lower than that under the series connection mode is that the former mode has a relatively smaller external resistance (seen from the single FPSG) and a larger available excitation voltage. Adjusting the external resistance to 15 Ω, the output electric power reaches a peak value at a relatively lower hot-end heating temperature compared with that in series mode, with an efficiency of the dual-opposed FPSG of 25.18%. The deviation in heat-to-electricity efficiency between experiments and simulations is within 2.7%. The displacement amplitude difference between the two power pistons is 0.15 mm, and the phase difference is 0.9 °. The displacement amplitude difference of the displacer is 0.01 mm, and the phase difference is 3.8 °. These test results indicate that a good operating consistency between the two single-piston FPSGs has been achieved under a parallel connection mode of the two linear alternators. However, series connection mode is less sensitive to in-consistency compared to the parallel connection mode. Therefore, we chose series electrical connection for the two linear alternators in the following tests and analysis.

The P-V diagram of the compression chamber of the dual-opposed FPSG, as observed in simulation and experiments, is depicted in Fig. 9. The energy conversion cycle associated with this configuration exhibits a pressure variation ranging from 4.4 MPa to approximately 5.6 MPa, with the compression volume varying from 6e-5 m³ to 1.25e-5 m³. The power generated by the FPSE can be calculated by the area enclosed within the curves. Notably, the power calculated by simulation is slightly less than that observed in experimental testing. However, the deviation between simulation and experiments remains within acceptable limits for engineering predictions.
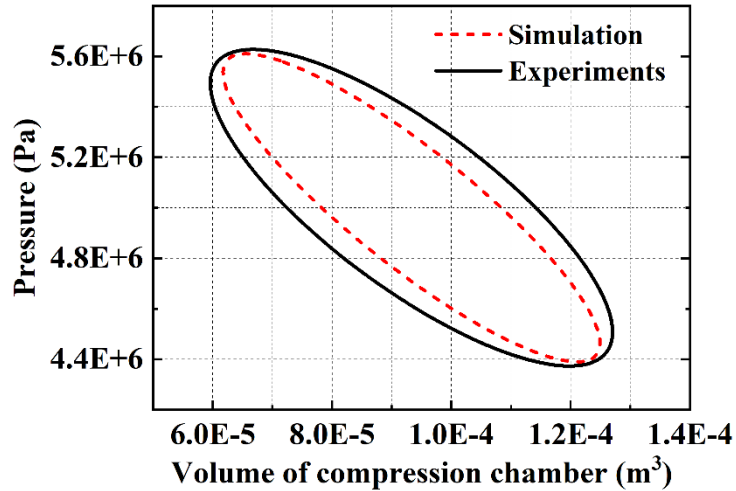
Figure 9 The P-V diagram of the dual-opposed FPSG in simulation and experiments

4.2 Effects of charge pressure

As mentioned before, the operating characteristics of dual-opposed FPSGs remain poorly understood. To solve this issue, this section presents the influence of different parameters such as charge pressure, load resistance, and external capacitance on the system performance. During the analysis, the design parameters are kept consistent with the data given in Table 1, except for the parameters used as variables in analysis processes.

As known in thermoacoustics, charge pressure is a key parameter of an acoustic resonance system, which directly impacts the impedance of the FPSE and loss pertinent to the clearance seal. Fig. 10 displays the wall temperature of hot end heat exchanger versus heating power at different charge pressures in experiments. Obviously seen that for a fixed charge pressure, the wall temperature of the hot end heat exchanger rises with the increase of heating power. If we keep the heating power as a constant, the wall temperature of the hot end heat exchanger drops with the increase of charge pressure. As indicated in Eq. (4) and Eq. (6), the acoustic impedance of the two linear alternators are merely related to the structural parameters of the alternator and external electricity circuit. If we fix the load resistance and external capacitance, the acoustic impedance of the linear alternators remains unchanged. However, an increase in the charge pressure of the system significantly increases the density of working fluid molecules and the amount of transmitted acoustic power, leading to the increase of the acoustic impedances of the FPSE. Consequently, to well match the acoustic impedance of FPSE and linear alternator, the

wall temperature of the hot end heat exchanger will decrease to abate the thermoacoustic effect under a same heating power.
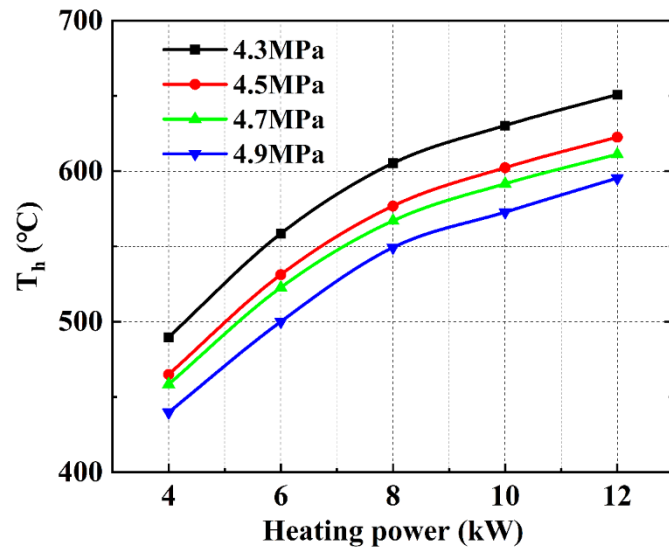

Figure 10 Wall temperature of hot end heat exchanger versus heating power at different charge pressure.

Fig.11 depicts the relationship between the electrical power output of two alternators and the charging pressure. Both alternators exhibit peak electrical power at 4.7 MPa within the tested range. The maximum difference in electrical power between the two alternators is 45 W. Additionally, as the charging pressure increases, the deviation between the two alternators decreases.
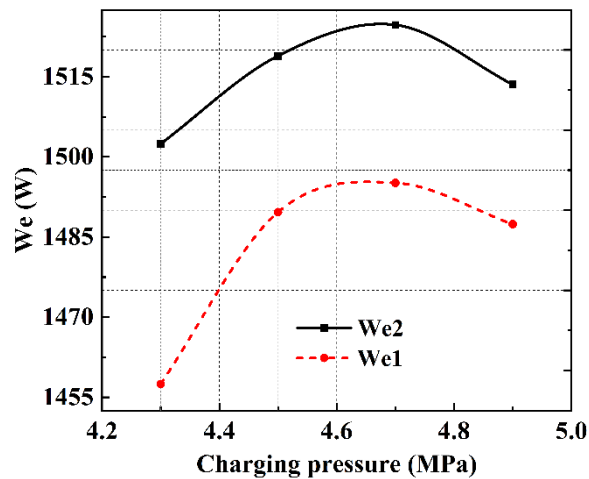
Figure 11 Electrical power output versus heating power at different charge pressure.

Fig.12 illustrates the phase difference of the two displacers and heat-to-electricity efficiency of the dual-opposed FPSG at different charge pressures. Within the test range, the

charge pressure exerts a positive impact on the heat-to-electricity efficiency when the charge pressure is below 4.7 MPa. Although heat-to-electricity efficiency increases with the rise of charge pressure, the growth in the clearance seal loss (gas leakage and mechanical damping coefficient) outweighs it, which leads to the decline of heat-to-electricity efficiency when the charge pressure is higher than 4.7 MPa, as indicated by the red line of Fig. 8. Meanwhile, the two displacers of the dual-opposed FPSG synchronize with the minimum phase difference at a charge pressure of 4.7 MPa. The inconsistency in movement of the two displacers may result from the inconsistent frictional resistance of gas bearings, which is related to charge pressure.
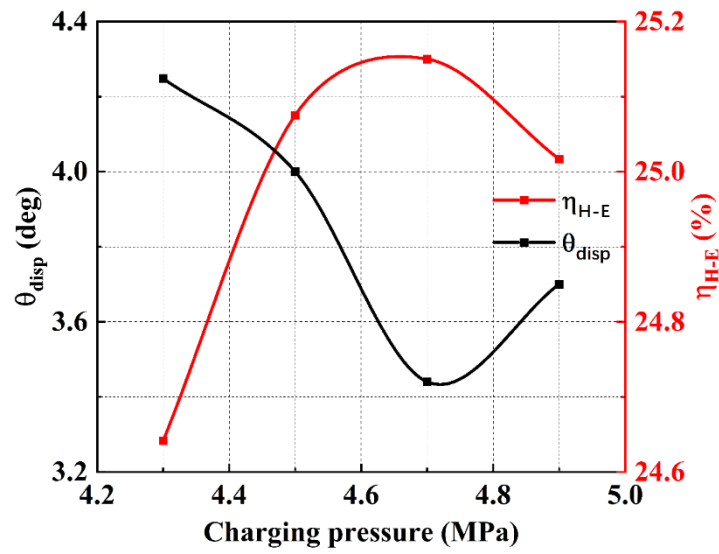
Figure 12 Phase difference of the two displacers and heat-to-electricity efficiency versus charge pressure.

The investigation into the onset and damping temperatures offers an intriguing perspective in thermoacoustics, where onset and damping temperatures are defined as the points at which the FPSG initiates and ceases its excited oscillation, respectively. Fig.13 shows the onset and damping temperatures versus charge pressure when the external resistance is 135 Ω. If gas expands isothermally in the expansion chamber in the onset process, its heat absorption, Q, and expansion work, W_e, can be expressed as:

$$Q = W_e = nRT \ln \frac{P}{P + \Delta p} \tag{13}$$

where Δp is the amplitude of oscillating pressure. According to Eq. (13), the expansion work produced to push the displacer will increase as the charge pressure ascends. Therefore, the onset temperature will decrease with the rise of charge pressure, shown as the black line in Fig. 9. In

addition, the damping temperature of the dual-opposed FPSG is influenced by the total dissipation of the system. At a charge pressure of 4.7 MPa, the system dissipation is minimized, resulting in the damping temperature reaching its lowest value (valley) at this pressure. The observation of higher damping temperatures compared to their onset counterparts aligns with the findings reported in Ref. [35].
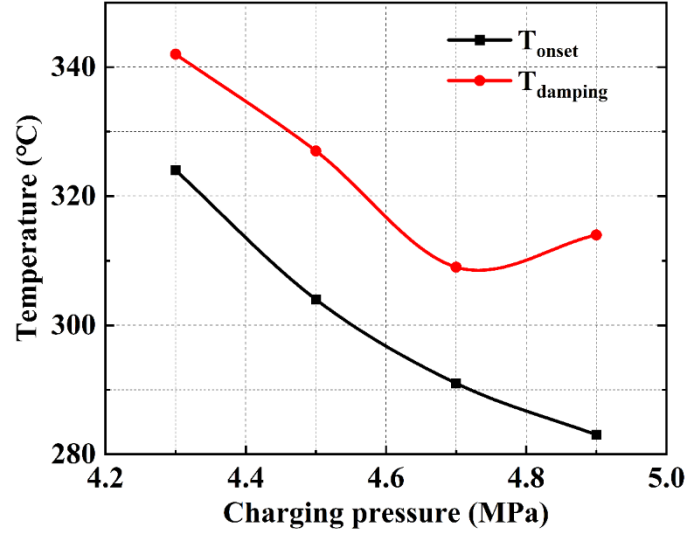

Figure 13 Onset and damping temperatures versus charge pressure

4.3 Effects of load resistance

In contrast to charge pressure, external electric impedance directly impacts the performance of the linear alternator as simply implied in the following Eq. (14). As a matter of fact, Eq. (14) is another form of Eq. (4) once electric resonance is achieved. The mechanism is quite straightforward that given a fixed acoustic impedance, a smaller load resistance contributes to a larger outcome of $\dfrac{Bl^2}{\dfrac{1}{2}R_{e-serial}+R_i}$, which embodies the electricity generation.

Herein for the dual-opposed FPSG, it's interesting to see how a common external electric impedance affects the performance of the entire system.

$$\left[Z_cA_pA_p-Z_bA_pA_p\right]_{serial}=\left[\frac{Bl^2}{\dfrac{1}{2}R_{e-serial}+R_i}+R_{mp}\right]+\left[m_p\omega-\frac{K_p}{\omega}\right]i \qquad (14)$$

Fig. 14 shows the variations of the hot end heat exchanger wall temperature and heat-to-electricity efficiency with external resistance at a heating power of 8 kW. Within the studied

range of load resistance in experiments, both the wall temperature of the hot end heat exchanger and the heat-to-electricity efficiency present a monotonic decrease trend with the increase of external electric resistance. For instance, if the load resistance increases from 45 Ω to 130 Ω, the wall temperature of the hot end heat exchanger and heat-to-electricity efficiency will dramatically decrease from 665 °C to 453 °C and from 25.76% to 16.11%, respectively.
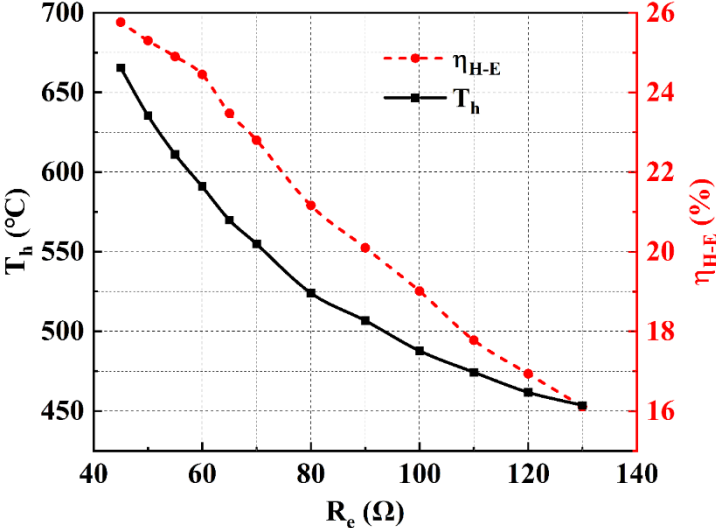

Figure 14 Wall temperature of hot end heat exchanger and heat-to-electricity efficiency versus external resistance.

Fig. 15 shows the dependence of current and power pistons displacement on the load resistance. The current amplitude depends on the force on the power piston, while the displacement amplitude of the power piston is related to the volume flow rate at the compression chamber. Consequently, an increase in the load resistance leads to a decrease in the current and displacement of the power piston. The displacement amplitude of the two power pistons changes synchronously but with a small deviation, and this displacement amplitude difference at a fixed external resistance might mainly be caused by the difference in the two linear alternators' internal resistance as derived from Eq. (2).
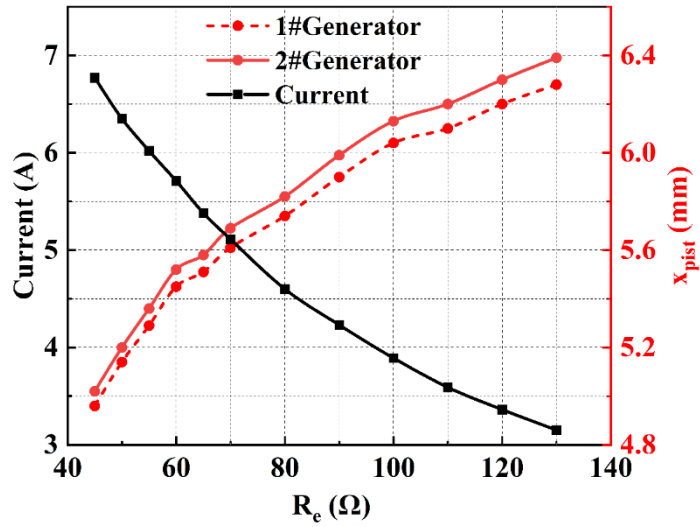
Figure 15 Current and power piston displacement versus external resistance.

Figure 16 depicts the relationship between electrical power output from two alternators and external resistance. With consistent heating power conditions, electrical power diminishes as resistance increases. This observation aligns with Eq. (3), where increased resistance correlates with reduced pressure fluctuations in the compression chamber, thereby weakening the alternators' power absorption capacity. Consequently, electrical power declines with higher external resistance. Notably, the consistency between the two FPSGs is excellent, with the difference in electrical power remaining within 2%.
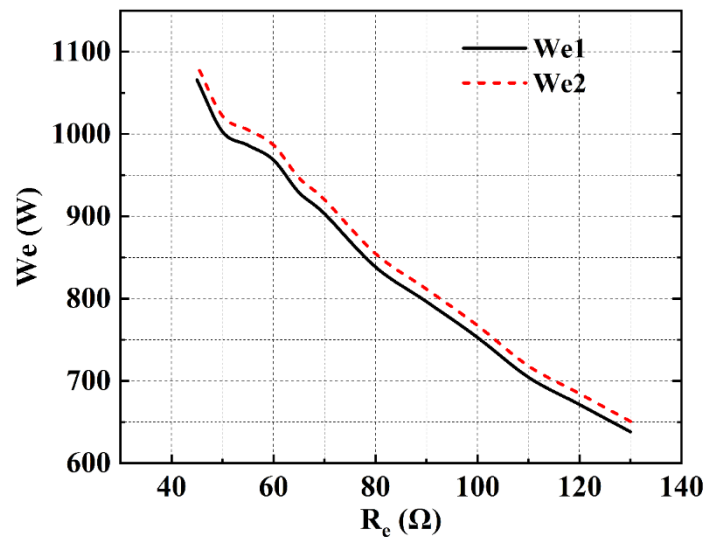
Figure 16 Current and power piston displacement versus external resistance.

4.4 Effects of external capacitance

In addition to load resistance, external capacitance influences indeed the acoustic impedance of the inlet of linear alternators and FPSG system's overall performance. Capacitance is a measure of a system's ability to store an electric charge, Fig. 17 illustrates the wall temperature of the hot end heat exchanger and electrical power at different external capacitances. As the capacitance increases, the wall temperature of hot end exchanger exhibit a peak value. Such a variation can be explained by deducing the relation between acoustic impedance and external capacitance. Multiplying both sides of Eq. (4) with the conjugate of the square of velocity $\hat{u}$ and using 1/2 Re() operator (Re() means taking the real part of a complex quantity) to calculate power flow, we have:

$$\frac{1}{2}\text{Re}\left[P_cU_P^* - P_bU_P^*\right]_{serial} = \frac{\frac{1}{2}U^2(\frac{1}{2}\text{R}_{e-serial} + R_i)}{(\frac{1}{2}\text{R}_{e-serial} + R_i)^2 + (\omega L - \frac{1}{2\omega C_{serial}})^2} + \frac{1}{2}\hat{u}^2R_{mp} \tag{15}$$

The left-side term of the equation is the acoustic power exerted on the power piston, and the first term on the right side is a form of electromagnetic work pertinent to external capacitance. An increase in the external capacitance will lead to the decrease of acoustic power exerted on the power piston after an initial increase to the peak point. Thus, the wall temperature of the hot end heat exchanger has peak value when Eq. (16) is satisfied.

$$\omega L - \frac{1}{2\omega C_{serial}} = 0 \tag{16}$$

Notable differences in variations are observed between the wall temperature of the hot end heat exchanger and electrical power after reaching their respective extreme capacitance points. Specifically, the decrease in electrical power exhibits a lesser magnitude compared to the decline in temperature of the hot end heat exchanger. This phenomenon is primarily attributed to the inconsistency in the optimal operating frequencies of the linear alternator and Free Piston Stirling Engine. Introducing higher capacitance mitigates the impact of the hot end heat exchanger temperature on electrical power, albeit at the expense of a slight reduction in thermal acoustic efficiency.
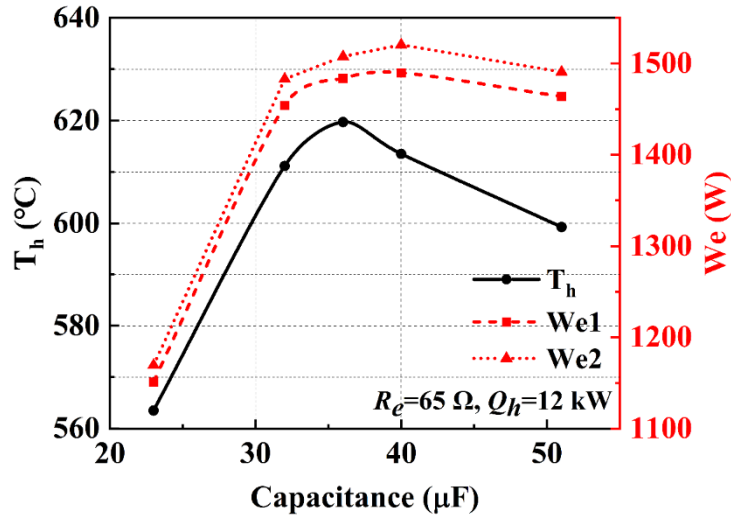
Figure 17 Wall temperature of hot end heat exchanger and electrical power versus external capacitance.

Fig. 18 shows the dependence of displacement amplitude of power piston (of one single-piston FPSG) on the external capacitance at different heating powers (8 kW, 10 kW and 12 kW). Likewise, an increase in the external capacitance leads to the change of the output acoustic impedance of the FPSE accordingly, as shown in Eq. (4), which consequently causes the displacement amplitude of the power piston to have a minimum value under different heating powers. Specifically, when the external capacitance is 32.6 µF, the displacement amplitude of the power piston reaches a minimum value of 4.72 mm at a heating power of 8 kW.
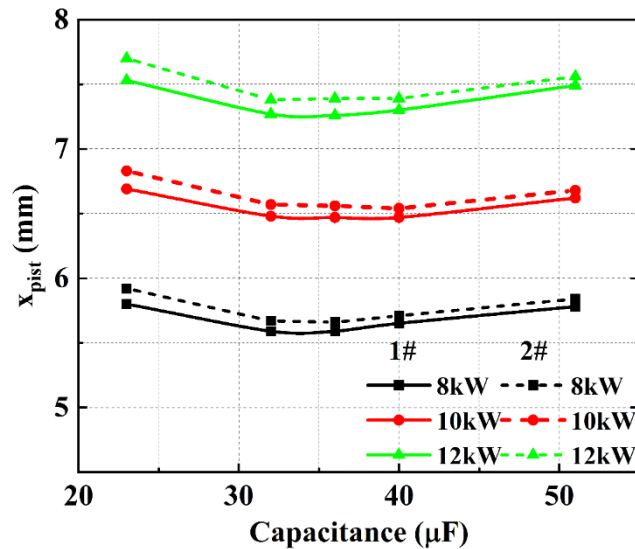
Figure 18 Displacement of the power piston versus external capacitance at different heating powers.

Fig. 19 displays the operating frequency versus heating power at different external capacitances. Within the studied range of external capacitance in experiments, for a fixed heating power, the frequency of the dual-opposed FPSG shows a monotonic increase trend with the increase of external capacitance. According to Eq. (17), we can obtain that $\omega^2 = 1/2LC_{serial}$, hence the increase in the external capacitance will lead to a increase of angular frequency ω.
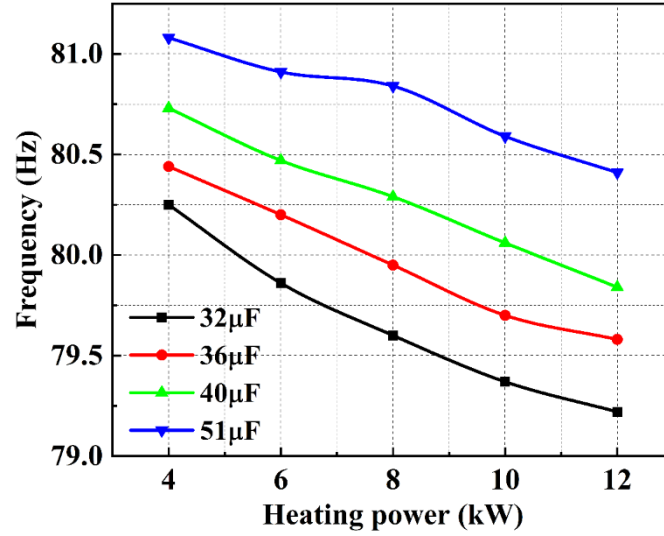

Figure 19 Frequency versus heating power at different external capacitances.

The dependence of onset and damping temperatures on external capacitance are given in Fig. 20. It can be seen from the black line in Fig. 20 that the larger the external capacitance, the higher the onset temperature, which is mainly attributed to the real part of the external electric load that increases with the external capacitance. Furthermore, within the test range of external capacitance, external capacitance exerts a negative impact on the damping temperature when the external capacitance is below 32.6 µF. The damping temperature has a minimum value when the external circuit is purely resistive, i.e., an external capacitance of 32.6 µF.
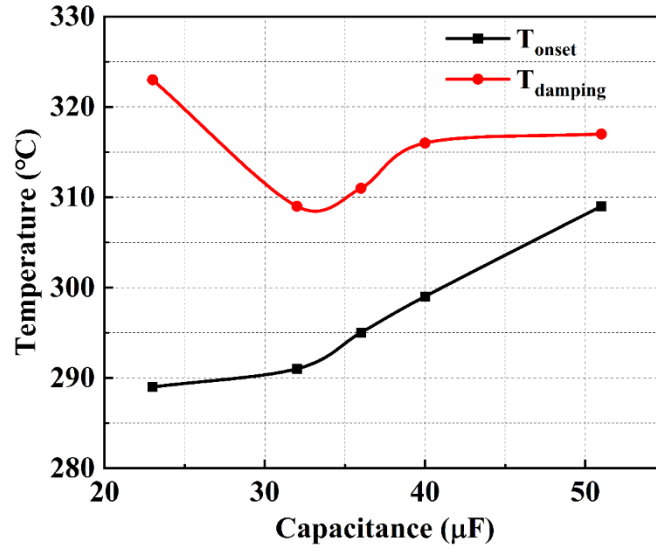
Figure 20 Onset and damping temperature versus external capacitance.

5. Conclusions

In this work, a 3-kW dual-opposed FPSG prototype which accommodates the heat pipes was designed, manufactured and studied. The prototype is composed of two identical 1.5 kW-class single-piston FPSG units sharing a common expansion chamber. A meticulous evaluation of the hot end heat exchanger was conducted and the results show an encouraging gas-solid temperature difference of 21 K. To gain a deep understanding of the linear alternators' electrical connection on the operation of the dual-opposed FPSG, the effects of series electrical connection and parallel electrical connection of liner alternators on the system performance were compared numerically and experimentally. Besides, the effects of charge pressure, load resistance, and external capacitance on the operation and system performance of the dual-opposed FPSG prototype were investigated via experiments.

The detailed comparison of experiments and calculations reveal that a good agreement has been achieved and the maximum deviation was within 5% in heat-to-electricity efficiency in different electrical connection modes. In experiments, the FPSG operated consistently and reached its rated power in both series connection and parallel connection modes with a heat-to-electricity efficiency around 25.2%. While the series connection mode outperforms the parallel connection mode in terms of sensitivity to in-consistency of the two single-piston FPSG units. In addition, the operating condition tests unveiled that with the decrease of charge pressure and load resistance, the wall temperature of the hot end heat exchanger increases gradually under a

fixed heating power. Owing to the fallout of heat pipe adaptive configuration, a larger volume of the expansion chamber is inevitable compared with a single-piston FPSG, and the optimal charge pressure of the dual-opposed FPSG drifts to 4.7 MPa when achieving the highest heat-to-electricity efficiency. Moreover, when the external circuit of the two alternators is purely resistive, both the wall temperature of the hot end heat exchanger and the heat-to-electricity efficiency reach peak values, and both the displacement amplitudes of the power piston and damping temperature have a minimum value. Although this preliminary work demonstrated a good consistency between two FPSG units, the underlying mechanism and parameter sensitivity are imperative to accomplishing high performance and zero vibration simultaneously, which is the objective of our future work.

Acknowledgements

Credit authorship contribution statement

Haojie Sun: Conceptualization, Modelling, Software, Formal analysis, Writing-original draft; **Guoyao Yu:** Funding Acquisition, Methodology, Writing- Review Editing, Supervision; **Dan Zhao:** Writing- Review Editing, Supervision; **Shunmin Zhu:** Writing- Review Editing; **Wei Dai:** Writing- Review Editing, Supervision; **Ercang Luo:** Conceptualization Supervision, Resources.

References

[1] C. Yang, N. Zhuang, H. Zhao, X. Tang, Dynamic performance of the combined stirling thermoelectric conversion technology for a lunar surface nuclear power system, Applied Thermal Engineering, 221 (2023) 119873. https://doi.org/10.1016/j.applthermaleng.2022.119873.

[2] J. Dyreby, J. Shumaker, K. E. Schaefer, J. Corey, J. J. Carroll, C. J. Chiara, G. Nellis, Assessment of the integration of a switched nuclear isomer material with a kinematic Stirling engine, Applied Thermal Engineering, 236 (2024) 121708. https://doi.org/10.1016/j.applthermaleng.2023.121708.

[3] T. Schneider, F. Ruf, D. Müller, J. Karl, Performance of a fluidized bed-fired Stirling engine as micro-scale combined heat and power system on wood pellets, Applied

Thermal Engineering, 189 (2021) 116712.
https://doi.org/10.1016/j.applthermaleng.2021.116712.

[4] Z. Jiang, G. Yu, S. Zhu, W. Dai, E. Luo, Advances on a free-piston Stirling engine-based micro-combined heat and power system, Applied Thermal Engineering, 217 (2022) 119187. https://doi.org/10.1016/j.applthermaleng.2022.119187.

[5] M.E. Zayed, J. Zhao, W. Li, A.H. Elsheikh, Z. Zhao, A. Khalil, H. Li, Performance prediction and techno-economic analysis of solar dish/stirling system for electricity generation, Applied Thermal Engineering, 164 (2020) 114427.
https://doi.org/10.1016/j.applthermaleng.2019.114427.

[6] T. Hussain, M.D. Islam, I. Kubo, T. Watanabe, Study of heat transfer through a cavity receiver for a solar powered advanced Stirling engine generator, Applied Thermal Engineering, 104 (2016) 751-757.
https://doi.org/10.1016/j.applthermaleng.2016.05.108.

[7] H.-S. Yang, Numerical model for predicting the performance and transient behavior of a gamma-type free piston Stirling engine, Applied Thermal Engineering, 185 (2021) 116375. https://doi.org/10.1016/j.applthermaleng.2020.116375.

[8] D. Sun, J. Zhang, S. Ge, Q. Shen, J. Linghu, Y. Qi, Operating characteristics of a 15 W free-piston Stirling generator, Applied Thermal Engineering, 211 (2022) 118412.
https://doi.org/10.1016/j.applthermaleng.2022.118412.

[9] Z. Jia, R. Wang, J. Hu, L. Zhang, Z. Wu, Y. Chen, E. Luo, Study on the coupling between engine and alternator in a free-piston Stirling generator, Applied Thermal Engineering, 217 (2022) 119222.
https://doi.org/10.1016/j.applthermaleng.2022.119222.

[10] A.T. Brown, Space power demonstrator engine-Phase I final report. NASA CR179555, Mechanical Technology Incorporated, Latham, New York, 1987.

[11] Schock A, Or C T, Kumar V. Radioisotope power system based on derivative of existing Stirling engine. 30th intersociety energy conversion engineering conference, 1995.

[12] Cockfield R D. Radioisotope power system options for future planetary missions. AIP Conference Proceedings, 2001: 740-746.

[13] Mason L S, Schreiber J G. A Historical Review of Brayton and Stirling Power Conversion Technologies for Space Applications. Space Nuclear Conference 2007.

[14] Kim S, Huth J, Wood J. Performance Characterization of Sunpower Free-Piston Stirling Engines. 3rd International Energy Conversion Engineering Conference, 2005.

[15] Briggs, Maxwell H , S. M. Geng , M. G. Robbie. Status of Kilowatt-Class Stirling Power Conversion Using a Pumped NaK Loop for Thermal Input - 7th International

Energy Conversion Engineering Conference, (2010).

[16] Briggs M H, Geng S M, Pearson J B, et al. Summary of Test Results From a 1 kWeClass Free-Piston Stirling Power Convertor Integrated With a Pumped NaK Loop.8th International Energy Conversion Engineering Conference, 2010.

[17] Wood J G, Stanley J. Free-Piston Stirling Power Conversion Unit for Fission Power System, Phase II Final Report. 2016.

[18] Wood J G, Buffalino A, Holliday E, et al. Free-Piston Stirling Power Conversion Unit for Fission Surface Power, Phase I Final Report. 2010.

[19] Gibson M A, Oleson S R, Poston D I, et al. NASA's Kilopower Reactor Development and the Path to Higher Power Missions. IEEE Aerospace Conference. 2017.

[20] Gibson M A, Poston D I, Mcclure P, et al. Kilopower Reactor Using Stirling TechnologY (KRUSTY) nuclear ground test results and lessons learned. 2018 International Energy Conversion Engineering Conference 2018.

[21] Lin M, Mou J, Chi C, et al. A space power system of free piston Stirling generator based on potassium heat pipe. Frontiers in Energy, 2020, 14(1): 1-10. https://link.springer.com/article/10.1007/s11708-019-0655-6.

[22] Dadd MW, Bailey PB, Davey G, et al. Vibration reduction in balanced linear compressors. Cryocoolers 2001;11:175–82. https://link.springer.com/chapter/10.1007/0-306-47112-4_23.

[23] Dang H. Development of high performance moving-coil linear compressors for space Stirling-type pulse tube cryocoolers. Cryogenics. 2015;68:1-18. https://doi.org/10.1016/j.cryogenics.2015.01.009.

[24] Park J, In S, Ko J, Kim H, Hong Y, Yeom H, et al. Development and parametric study of a 1kW class free-piston stirling cryocooler (FPSC) driven by a dual opposed linear compressor for LNG (Re)liquefaction. International Journal of Refrigeration. 2019;104:113-22. https://doi.org/10.1016/j.ijrefrig.2019.05.008.

[25] Park J, Ko J, Kim H, Hong Y, Yeom H, Park S, et al. The design and testing of a kW-class free-piston Stirling engine for micro-combined heat and power applications. Applied Thermal Engineering. 2020;164:114504. https://doi.org/10.1016/j.applthermaleng.2019.114504.

[26] M. Iguchi, M. Ohmi, K. Maegawa, Analysis of Free Oscillating Flow in a U-Shaped Tube, Jsme International Journal Series B-fluids and Thermal Engineering. 25 (1982) 1398-1405.

[27] D. Gedeon, Mean-Parameter Modeling of Oscillating Flow, Journal of Heat Transfer, 108 (1986) 513-518. https://doi.org/10.1115/1.3246964.

[28] S. Zhu, G. Yu, J. O, T. Xu, Z. Wu, W. Dai, E. Luo, Modeling and experimental

investigation of a free-piston Stirling engine-based micro-combined heat and power system, Applied Energy, 226 (2018) 522-533. https://doi.org/10.1016/j.apenergy.2018.05.122.

[29] S. Zhu, G. Yu, Y. Ma, Y. Cheng, Y. Wang, S. Yu, Z. Wu, W. Dai, E. Luo, A free-piston Stirling generator integrated with a parabolic trough collector for thermal-to-electric conversion of solar energy, Applied Energy, 242 (2019) 1248-1258. https://doi.org/10.1016/j.apenergy.2019.03.169.

[30] J. Luo, L. Zhang, Y. Chen, Y. Sun, G. Yu, J. Hu, E. Luo, Numerical study on a free-piston Stirling electric generator with a gas-spring-postpositioned displacer for high-power applications, Energy, 271 (2023) 127023. https://doi.org/10.1016/j.energy.2023.127023.

[31] L. Xiao, Z. Wu, Q. Zhu, Z. Jia, D. Zhao, J. Hu, S. Zhu, E. Luo, Dynamic response of a dual-opposed free-piston Stirling generator, Energy, 284 (2023) 129253. https://doi.org/10.1016/j.energy.2023.129253.

[32] Y. Chen, G. Yu, Y. Ma, J. Xue, F. Ahmed, Y. Cheng, H. Sun, S. Zhu, W. Dai, E. Luo, A thermally-coupled cascade free-piston Stirling engine-based cogeneration system, Applied Thermal Engineering, 236 (2024) 121679. https://doi.org/10.1016/j.applthermaleng.2023.121679.

[33] G.R. Dochat, Stirling space power demonstrator engine test/analytical comparison, Acta Astronautica, 15 (1987) 341-346. https://doi.org/10.1016/0094-5765(87)90169-X.

[34] Y. Qi, D. Sun, J. Zhang, Numerical study on a nuclear-powered Stirling system for space power generation, Applied Thermal Engineering, 233 (2023) 121140. https://doi.org/10.1016/j.applthermaleng.2023.121140.

[35] H. Sun, G. Yu, D. Zhao, W. Dai, E. Luo, Thermoacoustic hysteresis of a free-piston Stirling electric generator, Energy, 280 (2023) 128177. https://doi.org/10.1016/j.energy.2023.128177.